Nanoscale imaging of dopant incorporation in n-type and p-type GaN nanowires by scanning spreading resistance microscopy

Ece Aybeke, Alexandra-Madalina Siladie, Rémy Vermeersch, Eric Robin, Oleksandr Synhaivskyi, Bruno Gayral, Julien Pernot, Bruno Daudin, Georges Bremond

Journal of Applied Physics ARTICLE scitation.org/journal/jap

Nanoscale imaging of dopant incorporation in n-type and p-type GaN nanowires by scanning spreading resistance microscopy

Cite as: J. Appl. Phys. **131**, 075701 (2022); doi: 10.1063/5.0080713
Submitted: 2 December 2021 · Accepted: 30 January 2022 ·
Published Online: 15 February 2022

Ece N. Aybeke,[1,2,a)] Alexandra-Madalina Siladie,[2] Rémy Vermeersch,[2] Eric Robin,[3] Oleksandr Synhaivskyi,[1] Bruno Gayral,[2] Julien Pernot,[4] Georges Brémond,[1,a)] and Bruno Daudin[2,a)]

AFFILIATIONS

[1]Université de Lyon, Institut des Nanotechnologies de Lyon, UMR 5270 CNRS, INSA de Lyon, 7 Avenue Jean Capelle, 69621 Villeurbanne cedex, France
[2]Univ. Grenoble Alpes, CEA, IRIG-PHELIQS, NPSC, 17 Rue des Martyrs, 38000 Grenoble, France
[3]Univ. Grenoble Alpes, CEA, IRIG-MEM, LEMMA, 17 Rue des Martyrs, 38000 Grenoble, France
[4]Univ. Grenoble Alpes, Grenoble INP, Institut Néel, CNRS, 38000 Grenoble, France

[a)]**Authors to whom correspondence should be addressed:** eaybeke@gmail.com; georges.bremond@insa-lyon.fr; and bruno.daudin@cea.fr

ABSTRACT

The realization of practical semiconductor nanowire optoelectronic devices requires controlling their electrical transport properties, which are affected by their large surface/volume ratio value and potentially inhomogeneous electrical dopant distribution. In this article, the local carrier density in Si-doped and Mg-doped GaN nanowires grown catalyst-free by molecular beam epitaxy was quantitatively measured using scanning spreading resistance microscopy. A conductive shell surrounding a more resistive core was observed in Mg-doped, p-type GaN nanowires, balancing the formation of a depleted layer associated with sidewall surface states. The formation of this conductive layer is assigned to the peripheral accumulation of Mg dopants up to values in the 10^{20} /cm^3 range, as determined by quantitative energy dispersive x ray spectroscopy measurements. By contrast, Si-doped n-type GaN nanowires exhibit a resistive shell, consistent with the formation of a depleted layer, and a conductive core exhibiting a decreasing resistivity for increasing Si doping level.

I. INTRODUCTION

With a bandgap value range extending from infrared to ultraviolet (UV), the III-nitride semiconductor family, i.e., InN, GaN, AlN, and their ternary or quaternary alloys are now currently used for visible and UV light emitting devices (LEDs) applications. More recently, the continuous progress in epitaxial growth techniques has motivated an increased interest in III-nitride nanowires (NWs) to improve such devices.[1,2] As a matter of fact, the specificities of NWs with respect to 2D epilayers, namely, their remarkable crystallographic qualities and the propensity of the NW heterostructures to elastically relax rather than plastically,[3,4] opened the path to the realization of visible LEDs beyond the so-called green gap.[5,6] For the same reasons, AlGaN/AlN NW heterostructures are now considered as a realistic alternative to planar UV LEDs.[7]

Remarkably, it was established that n-type doping level of GaN NWs (using Si) can be significantly increased with respect to layers, which was assigned to the higher Si dopant solubility limit in GaN NWs.[8] In addition, specific features such as an increased Mg incorporation in GaN NWs through the m-plane sidewalls were identified, making NWs very promising for the realization of LEDs.[9] Finally, the recent demonstration that In–Mg co-doping of AlN NWs led to a drastic increase of Mg content in AlN NWs and to the concomitant improvement of electrical transport properties has opened the path to the realization of efficient UV-C LEDs.[10]

Concerning the electrical doping properties, the carrier concentration in four probe contacted single Si-doped GaN NWs was reported by Mansfield *et al.* and by Fang *et al.*[8,11] Also, time resolved photoconductivity measurements were performed on

single Si-doped GaN NWs to extract both charge carrier lifetime and mobility.[12] As concerns p-type GaN NWs, the determination of doping level in Mg-doped NWs by photochemical measurements was recently reported by Kamimura *et al.*[13]

In spite of these progresses, the detailed analysis of nitride NWs electrical properties still needs to be developed. Standard Hall effect measurement techniques widely used for the characterization of 2D layer electrical properties are not applicable to NWs in the general case due to their peculiar geometry and small size. Four point probe resistivity measurements are very challenging for the same reasons while not providing an independent determination of both carrier concentration and mobility. Also, it has to be pointed out that the electrical characterization of single NWs, because being time costly and challenging, prevents from obtaining the statistical information, which could be extrapolated to the huge number of NWs in a single LED, making desirable direct information on large arrays of NWs.

Among the doping characterization techniques of semiconductors, scanning spreading resistance microscopy (SSRM) is an electrical characterization technique based on atomic force microscopy (AFM). Basically, the sample surface is scanned over by a hard conductive AFM probe while applying an additional DC bias on the sample. The spreading resistance is measured using a logarithmic current amplifier in order to keep a large dynamic range.[14–16] SSRM provides two-dimensional carrier profiling of semiconductors in a concentration range from 10^{16} to 10^{20} at/cm^3 with a high spatial resolution (sub 10 nm).[17] A few studies to date have reported the use of SSRM to determine the electrical properties of an ensemble of Si or ZnO NWs[18–20] while such studies have not been conducted for GaN NWs. Accordingly, it is the goal of the present article to study the electrical properties of arrays of n-type and p-type doped GaN NWs combined with spreading resistance mapping at the scale of single NWs to probe local carrier distribution. For both n-type and p-type doped GaN NWs, inhomogeneities in carrier distribution along the diameter section of NWs were put in evidence by local resistivity mapping, which were clearly assigned to inhomogeneous dopant distribution.

II. RESULTS AND DISCUSSIONS

A. Growth of GaN NWs and planarization process of samples

The doped GaN NWs under consideration in the present study are typically 1 μm long and 100 nm wide. They were grown catalyst-free by plasma-assisted molecular beam epitaxy (PA-MBE). The substrate was Si (111). After standard de-oxidization in 10% HF solution, the 2–in. Si (111) wafers were mounted In-free on a molybdenum sample holder. Following a two-step outgassing procedure at 300 and 800 °C, the growth of spontaneously nucleated GaN NWs was carried out. n-type doping was achieved by exposing the sample to a Si flux during growth. Different doping levels were obtained by varying the temperature of the Si effusion cell between 900 and 938 °C. p-type doping was achieved using a Mg effusion cell.

The length of NWs varies in function of growth temperature and the dispersion of length can reach hundreds of nanometers, especially at high temperatures (> 795 °C).[8,21] The scanning electron microscope (SEM) images shown in Fig. 1 were performed in cross section (90° tilt angle) using a 5 mm working distance and a 5 kV acceleration voltage to avoid charging effect.

In order to limit the dispersion length to some tens of nanometers [see Fig. 1(a)], the growth temperature was fixed to 790° for both Si-doped and Mg-doped GaN NWs. Even if reduced, such NW height dispersion is undesired because the high contact force ($\geq \mu$N) applied during SSRM measurement may damage the sample as well as the probe. Therefore, we applied a planarization process, as described in more detail in the supplementary material. The purpose of this planarization process is to fill the gap between

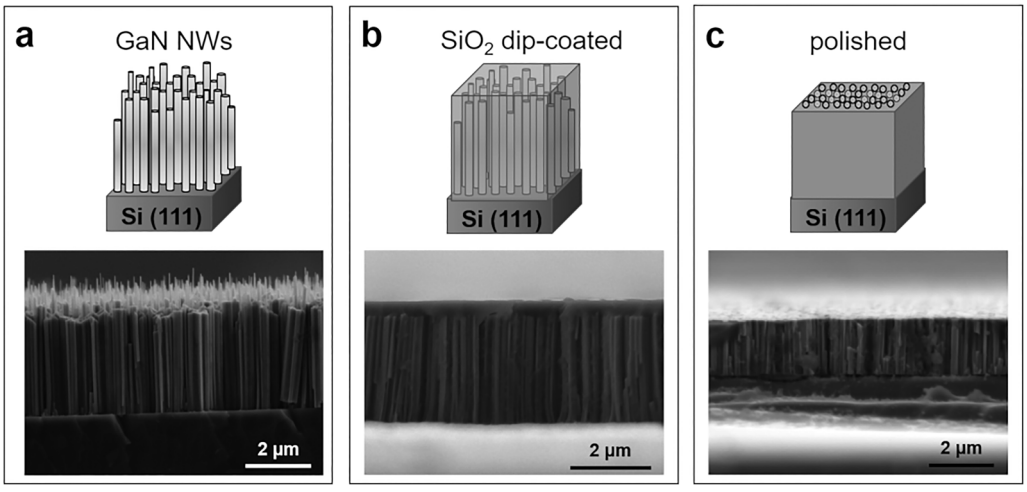

FIG. 1. Planarization process for GaN NWs. Schematic presentation and corresponding SEM images of (a) as-grown, (b) SiO_2 dip-coated, and (c) polished GaN NWs samples.

NWs with insulating material (SiO_2) and equalize the length of the NWs, as shown in Figs. 1(b) and 1(c), respectively, after a smooth polishing of the surface.

B. Si and Mg incorporation in GaN NWs

The chemical doping regime of NWs obeys specific mechanisms, intrinsically related to the geometry of these nano-objects and their growth mode. For both Si and Mg, the increase of the dopant species flux eventually induces a decrease in the axial GaN NW growth rate and a simultaneous increase of their diameter.[22] Furthermore, for moderate Si fluxes, the Si incorporates homogeneously along the diameter of GaN NWs.[8] However, for a high enough Si flux, the formation of a Si-rich defective shell is observed in Si-doped GaN NWs, assigned to the relaxation of the tensile strain induced by Si doping. In the case of Mg-doped GaN NWs, a recent atom probe tomography study put in evidence a radial Mg gradient.[9] This gradient was assigned to the H-enhanced stabilization of the Mg-rich reconstruction of the m-plane sidewall surface[23] associated with an increased Mg diffusion rate from sidewalls toward the NW core. The resulting formation of a Mg-enriched shell around a less Mg-doped core is expected to significantly affect the electrical transport properties of NW-based devices.

In addition to the inhomogeneous distribution of doping impurities along the radius, the distribution of charge carriers themselves is governed by the existence of a surface depletion region assigned to the Fermi level pinning by surface states.[24] For n-type GaN NWs, surface depletion results in the formation of a conducting core surrounded by a depleted shell.[25,26] The size of both the conducting core and the depleted shell is depending on the doping level and on the NW diameter. For a small enough diameter and low doping, the entire NW can be depleted from free carriers. By contrast, for larger diameters and high doping level, the depleted area is limited (few tens of nm depending of the doping) to a thin shell around a conducting core. In the case of an inhomogeneous chemical dopant distribution, the situation is qualitatively unchanged although it may be significantly intensified, depending on the details of the dopant profile.[27] Similarly, for p-type GaN NWs, the band bending induced by the lateral surface states is expected to result in hole accumulation in the NW core and to the formation of a depleted shell.

C. Monitoring Mg gradient in p-type GaN NWs

Figure 2 presents a typical SSRM analysis of p-type GaN NW arrays. The experiments were carried out using a Dimension 3100 microscope equipped with Nanoscope™ V (Bruker, Santa Barbara, CA, USA). All the electrical measurements were carried out with a commercial electrical SSRM mode. The topography and resistance images were collected in $2 \times 1\,\mu m^2$ of scan size and 0.7 Hz of scan rate in high resolution (512×256 pixel^2) using the contact mode. The tracking force was fixed to $\sim 1.4\,\mu N$ to provide a good contact without damaging sample surface. In order to eliminate scanning artifacts due to surface morphology or scanning direction or step height at edge, the surfaces of samples were scanned in trace and retrace directions with a conductive, highly doped (3–5 mΩcm)

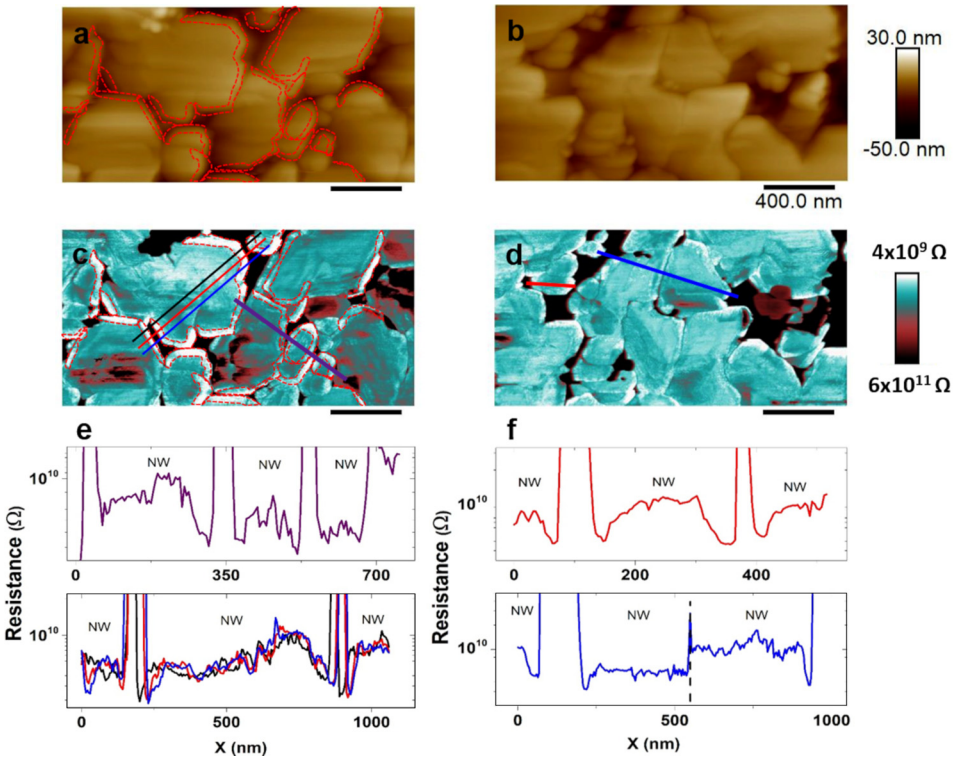

FIG. 2. (a) and (b) Topography and (c) and (d) resistance images of Mg-doped, p-type GaN nanowires. Scale bars = 400 nm. (e) and (f) Corresponding resistance profiles along the lines in resistance images. The corresponding height scale (color bar) is presented on the right side of AFM images. For SSRM images, dark and bright colors indicate high and low resistance values, respectively, according to the color scale shown on the right.

diamond coated cantilever with spring constant of 42 N/m (CDT-NCHR, Nanosensors) in ambient conditions at room temperature of 21 °C (see Fig. S1 in the supplementary material). The nominal resistance of tip does not exceed 10 kΩ, which allows neglecting the resistance of the probe since the measured resistance is higher than at least three orders of magnitude. The topography images of p-type GaN NWs are presented in Figs. 2(a) and 2(b). The NWs were found mostly coalesced with their radius varying from 70 to 600 nm, whereas the diameter of unprocessed NWs is in the 50–70 nm range, suggesting that nanowires collapse during planarization process.

When a NW is under SSRM analysis, the total measured resistance corresponds to a serial resistor including the resistance of the probe R_{tip}, the local spreading resistance R_S, the resistance of nanowire R_{NW}, and the bulk resistance of sample R_{bulk}. However, the measured resistance is dominated by the spreading resistance, R_S, if the contact between the tip and sample is considered to be ohmic, i.e., having linear current–voltage characteristic. The ohmic nanocontact model is more appropriate when highly doped materials (above 10^{18} at/cm^3) are under investigation, which is what is targeted in this study. Previous studies have detailed physics of SSRM and the case of NW analysis.[16,18,19,28] In the case where the mean free path of the electrons λ is much larger than the contact radius α, the local spreading resistance determined by Sharvin's law is $R_s = \frac{4\rho\lambda}{(3\pi\alpha^2)}$, where ρ, λ, and α are the sample resistivity, the electron mean free path, and the tip–sample nanocontact area radius, respectively. The resistivity is defined as $\rho = 1/(qn\mu_n + qp\mu_p)$, where μ is the carrier mobility and n and p are the concentration of electrons and holes, respectively. Thereby, SSRM provides the local carrier concentration in a nanoscale volume.

A constant bias voltage V_{DC} was applied between the tip and sample to measure the spreading resistance. Contrary to the case of Si structures or compounds such as GaAs or InP, SSRM measurements in the case of GaN require the application of high sample bias voltage.[29] By varying V_{DC} from −4 to 4 V, it was found that the optimal bias value was $V_{DC} = 3.5$ V. All resistance images were collected with this bias value for p-type and n-type GaN samples. The resistance images obtained using such an optimized bias display a clear contrast between GaN NWs and the SiO_2 matrix, as shown in Figs. 2(c) and 2(d), where GaN NWs correspond to light color and are surrounded by black areas corresponding to a highly resistive SiO_2 matrix. Some lighter areas exhibiting low local spreading resistance values are highlighted by dashed lines on both topography and resistance images [Figs. 2(a) and 2(c)] of NWs. The width of these low resistivity peripheral areas is 46 ± 8 nm. The resistance profiles presented in Fig. 2(e) indicate that the NWs have similar average resistance values ∼5×10^9 Ω and are separated by more resistive (≥10^{12} Ω) SiO_2 matrix. More precisely, Fig. 2(f) shows the lateral resistance profile of a single NW (red line). The resistance value is 3.3–3.7 × 10^9 Ω at the periphery while it is 1.2×10^{10} Ω at the center of the NW. Interestingly, in Fig. 2(f), which corresponds to two NWs coalesced during the growth, no clear resistance drop is visible close to the coalescence line, suggesting different dopant incorporation regimes for coalesced and un-coalesced NWs.

The experimental evidence in Mg-doped GaN NWs of a thin shell exhibiting a low local spreading resistance value is in apparent contradiction with the generally expected formation of a depleted shell due to Fermi level surface pinning. The question then arises whether this feature could be assigned to the radial Mg gradient decreasing from the side to the center and, more precisely, to determine whether the expected Mg gradient could be strong enough to counter-balance the surface depletion mechanism. Energy dispersive x-ray spectroscopy (EDX) experiments were performed to address this issue, in order to quantitatively analyze the Mg distribution at the nm scale in the Mg-doped NWs (see the supplementary material). Figure 3 shows the results obtained in the region corresponding to the SSRM experiments in Fig. 2. A marked Mg gradient profile from periphery to center of the NW shown in Fig. 3(a) is put in evidence in Fig. 3(b), assessing a Mg concentration of about ∼2×10^{20} /cm^3 in periphery, five times higher than in the NW center where the Mg content was ∼4×10^{19} /cm^3. A large dispersion of the Mg content was observed from NW to NW. For the NW shown in Fig. 3(c), the Mg concentration is about ∼4×10^{20} /cm^3 in the upper left side of periphery [see Fig. 3(d)]. By contrast, the Mg concentration in the lower right periphery of this NW is comparable to the concentration in the center, i.e., below the 10^{19} /cm^3 detection limit.

Although the Mg detection limit by EDX (about 1×10^{19} /cm^3) prevents from precisely determining the Mg concentration in the center of NWs, it appears that the Mg concentration in the periphery is at least 4–40 times higher than in the core, in the 10^{20} /cm^3 range, with a large variability from NW to NW. If considering that the effective acceptor ionization energy is significantly decreasing for such Mg concentrations,[30] an even larger free carrier ratio between periphery and center should be expected. However, the resistance value is about four times smaller at the periphery than at the center of the NW. As the free carrier concentration is directly related to SSRM value, this suggests that the Mg dopant concentration enhancement in periphery could be partially balanced by the presence of a depleted shell resulting from surface band bending, leading to a reduced carrier gradient with respect to the Mg concentration gradient from periphery to center.

To assess this hypothesis, the carrier density distribution resulting from the inhomogeneous Mg distribution was calculated using the NextNano software and presented in Figs. 3(e) and 3(f). Numerical simulations were performed using Poisson equation solver with standard materials parameters. NW was defined as a two-dimensional regular GaN hexagon. The whole structure was enclosed in air and the Fermi level was pinned on all GaN/air interfaces as described in Fig. 3. The Mg acceptor density in the core was set at 5×10^{19} /cm^3 with an ionization energy value of 130 meV. The Mg acceptor density in the 40 nm thick shell was fixed to 2×10^{20} /cm^3 with an ionization energy value of 70 meV[30] [Fig. 3(f), red dashed line]. Assuming a midgap Fermi level pinning at 1.7 eV above the topmost of the valence band, the results displayed in Figs. 3(e) and 3(f) put in evidence a shell carrier density of 1.1×10^{19} /cm^3, which drops at 2×10^{18} /cm^3 in the core. Interestingly, the shell carrier density is poorly affected by the presence of a thin depleted layer, whatever the Fermi level pinning, corresponding to a 2.5 nm thickness for a midgap Fermi level pinning. As such a depleted layer thickness is far smaller than the lateral resolution of the SSRM experiment, about 10 nm,[17] the shell conductivity is dominated by the radial gradient of Mg

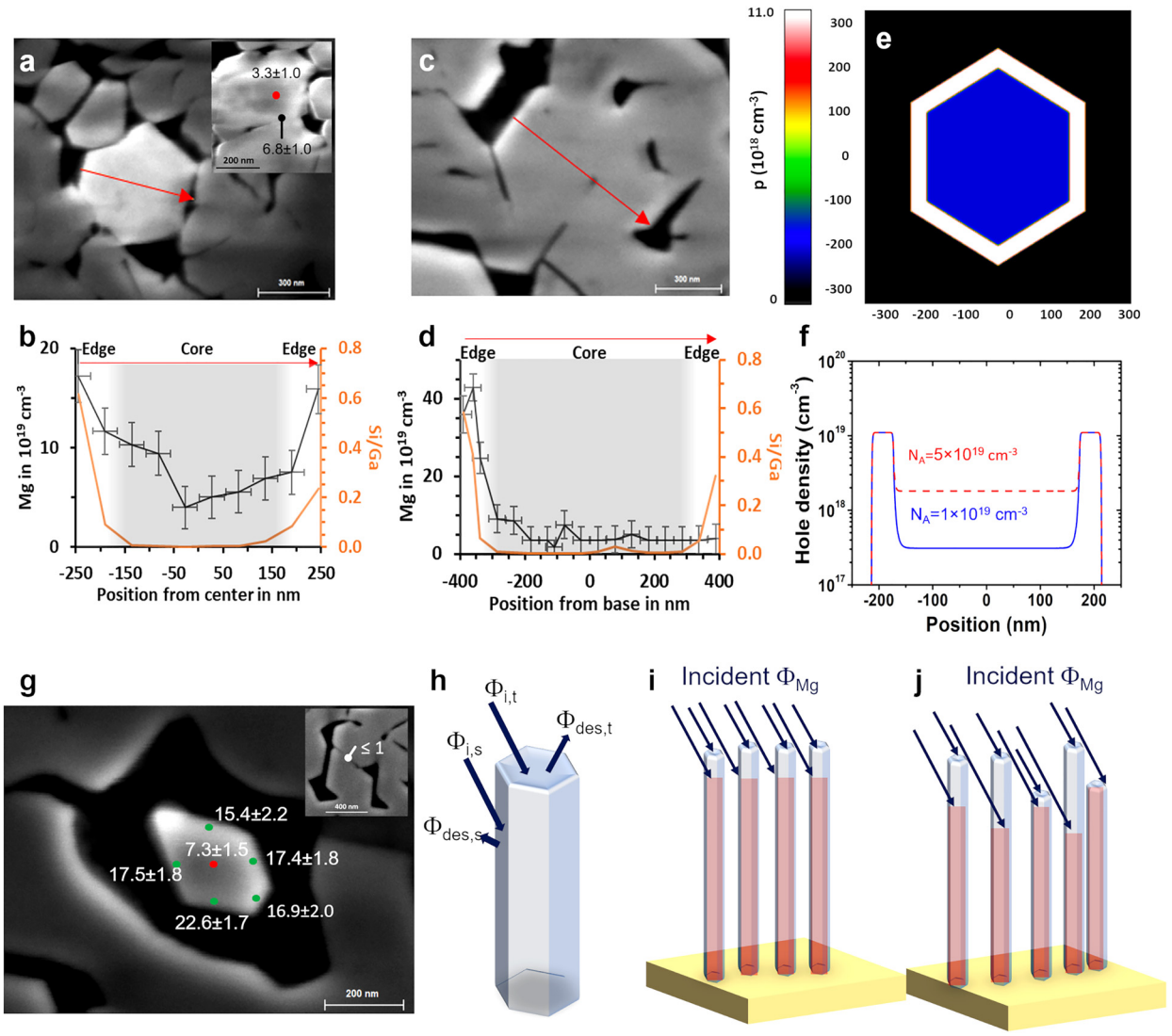

FIG. 3. EDX analysis of the Mg content in NWs in the same area as the one used for SSRM experiments. (a) SEM image and EDX analysis of the Mg content in a NW high density area, close to the Si wafer edge. Inset: Mg content (in 10^{19} /cm^3 units) in the center (red dot) and the coalescence zone (black dot) of two NWs. (b) Profile along the red arrow in (a). (c) SEM image of two coalesced NWs in a zone closer to the Si wafer center, (d) profile along the red arrow in (c), emphasizing the asymmetry of Mg distribution. (e) Calculated free hole density within the plane perpendicular to the NW growth axis. The Mg acceptor density in the core was set at 5×10^{19} /cm^3 with an ionization energy value of 130 meV. The Mg acceptor density in the 40 nm thick shell was fixed to 2×10^{20} /cm^3, with an ionization energy value of 70 meV. A midgap Fermi level pinning at 1.7 eV above the topmost of the valence band is assumed. (f) Free hole density profile along the x = 0 axis from (e) (red dashed line) and same calculation except the Mg acceptor density in the core set at 1×10^{19} /cm^3 with an ionization energy value of 180 meV (full blue line). (g) Mg content (in 10^{19} /cm^3 units) in the center (red dot) of an isolated NW and close to the edges (green dots). Inset: the Mg content is lower than the 10^{19} /cm^3 detection limit in the coalescence zone (white dot) of two NWs. (h) Schematics of Mg incorporation process during GaN NW growth. $\Phi_{i,t}$ and $\Phi_{i,s}$ are the Mg fluxes impinging on top and sidewall, respectively. $\Phi_{des,t}$ and $\Phi_{des,s}$ are the Mg fluxes desorbing from top and sidewall. (i) In the case of regularly spaced NWs, both $\Phi_{i,t}$ and $\Phi_{i,s}$ are the same for all NWs leading to a similar shadowed area (orange). (j) In the case of irregularly spaced NWs exhibiting height dispersion, shadow effect associated with highest NWs may prevent Mg flux to reach the sidewall of close by and shorter adjacent NWs as schematized.

content. However, the free carrier shell/core ratio value extracted from Fig. 3(f), about 5, is in good agreement with the ratio of 4 found for the shell/core resistance. Another example is shown in Fig. 3(f) with the same parameters, except the Mg acceptor core density value which has been set to the EDX detection limit value, i.e., 1.0×10^{19} /cm^3, associated with an ionization energy of 180 meV. In this case, the free carrier shell/core ratio value amounts to about 30, significantly higher than the shell/core

resistance values extracted from data in Fig. 2. This discrepancy is tentatively assigned to the fact that the current is indeed flowing through a non-uniformly doped area consisting of adjacent high and low resistivity regions due to the lateral resolution imposed by the AFM diamond tip. As a consequence, the current line flowing from tip might follow a path through the lower resistivity region, leading to an underestimation of the core resistance of the Mg-doped GaN NWs as we observe.

If now analyzing an isolated NW in the same area [Fig. 3(g)] and by contrast to asymmetric Mg content distribution observed in Fig. 3(d), the Mg amount is found higher than in the center close to *each* of the edges, suggesting that the Mg content is depending on the NW surface coverage in the analyzed region. Furthermore, the Mg amount in a point close to the coalescence region of two adjacent NWs was either similar to the value in the center, i.e., below the detection limit [inset of Fig. 3(g)] or far higher as shown in the inset of Fig. 3(a), which refers to a region of the sample closer to Si wafer edge. In this last case, it suggests that Mg was preferentially incorporated in the periphery *before coalescence* as in the case of the isolated NW in Fig. 3(c). It furthermore supports the fact that coalescence was posterior to growth and resulted from the planarization process, as inferred from the comparison between SEM images of as-grown and planarized NWs in Fig. 1. By contrast, in the case of the inset in Fig. 3(g), the low Mg content in the coalescence region suggests an inhomogeneous Mg gradient profile in each of the coalesced NWs, consistent with results in Fig. 3(d).

For a region of the sample closer to Si wafer edge, a Mg concentration of about $2–6 \times 10^{20}$ /cm^3 is found in periphery of the NWs [see Figs. 3(a) and 3(b)]. The Mg concentration in the NW central part is still lower than in periphery. However, it may reach 5×10^{19} /cm^3 or more, which is assigned to a lower desorption rate from the top surface. This feature is related to the presence of a temperature gradient decreasing from center to edge of the 2-in, free-standing Si substrate. The Mg dopant desorbing flux from the NW top, $\Phi_{des,t}$, is expected to be drastically affected by such a growth temperature gradient through the temperature-activated Mg desorption process. By contrast, the Mg coverage rate on the sidewall is stabilized by the formation of a H–Mg reconstruction,[9,23] making the Mg dopant desorbing flux from the NW sidewalls, $\Phi_{des,s}$, less sensitive to the growth temperature value.

The variability of Mg content close to NW edges in all analyzed areas is tentatively assigned to a shadow effect, which depends on the local NW density and may prevent the Mg flux to reach the sidewalls when NWs are close one to each other. As schematized in Fig. 3(h), the Mg flux consists of two contributions, namely, $\Phi_{i,t}$ and $\Phi_{i,s}$ impinging on top surface and sidewalls, respectively. In the general case of a Mg sticking coefficient <1, a fraction of Mg atoms adsorbed on the surface may next be

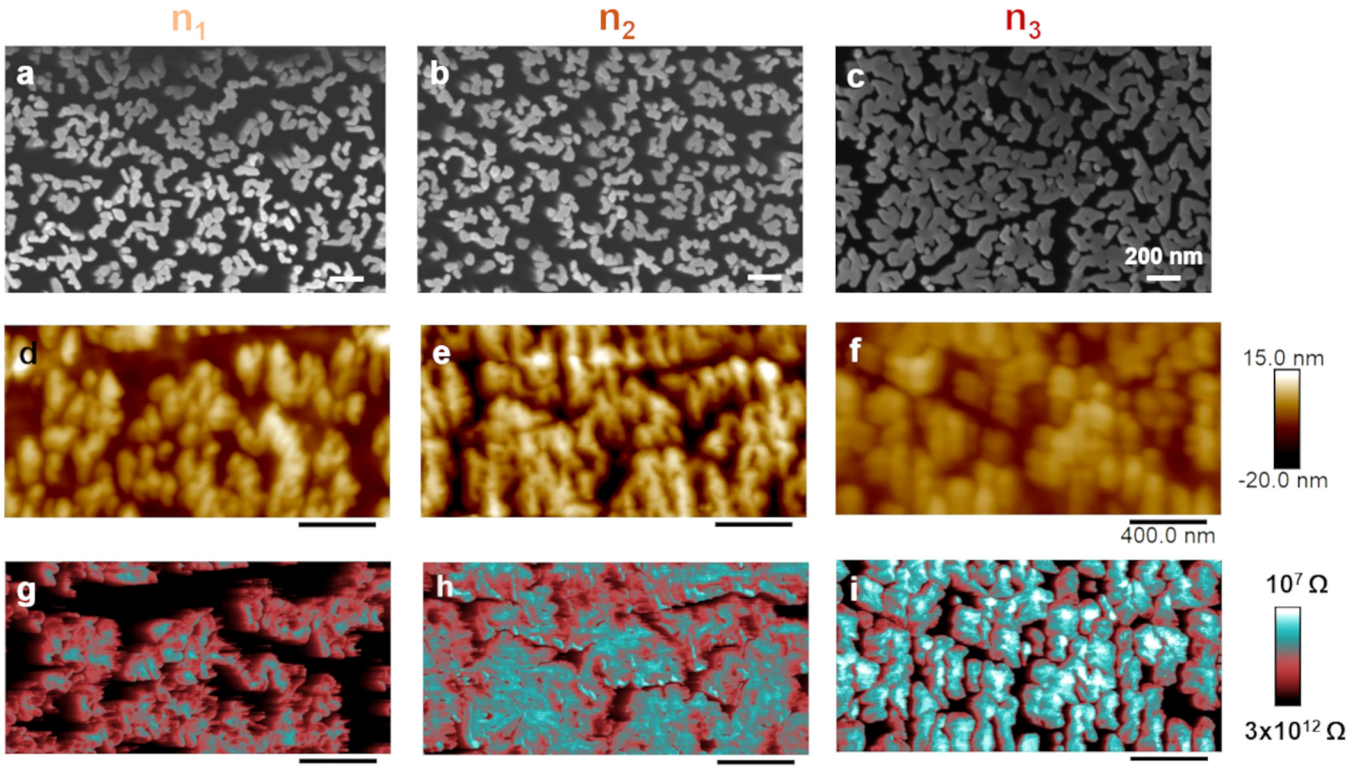

FIG. 4. SEM and SSRM analysis of Si-doped, n-type GaN NWs. SEM images [(a)–(c)], topography images [(d)–(f)], and resistance images [(g)–(i)] of n-type GaN NWs with Si cell temperature of 900 (n_1), 920 (n_2), and 938 °C (n_3), respectively. Scale bars are 200 and 400 nm for SEM [(a)–(c)] and AFM [(d)–(i)] images, respectively.

desorbed, corresponding to $\Phi_{des,t}$ and $\Phi_{des,s}$, respectively. It was previously established that Mg incorporation through lateral facets was indeed favored, leading to a radial Mg gradient decreasing from the side to the center.[9] As schematized in Figs. 3(i) and 3(j), the amount of Mg actually reaching the sidewalls depends on such a shadow effect. In the case of regularly spaced NWs [Fig. 4(i)], both $\Phi_{i,t}$ and $\Phi_{i,s}$ are the same for all NWs, leading to a similar shadowed area. However, in the case of irregularly spaced NWs exhibiting height dispersion, shadow effect associated with highest NWs may prevent Mg flux to reach the sidewall of close by and shorter adjacent NWs.

D. Impact of Si flux on the electrical properties of n-type GaN NWs

As concerns n-type doping using Si, three GaN NWs samples with Si cell temperature of 900 (n_1), 920 (n_2) and 938 °C (n_3) were investigated. First, we investigated the morphological features of Si-doped NWs by SEM [Figs. 4(a)–4(c)] and AFM topography [Figs. 4(d)–4(f)] images. Then, we compared the electrical properties of these NWs as a function of Si doping (Si cell temperature). Interestingly, the SSRM experiments reported here have put in evidence inhomogeneities in the current flow, consistent with the expected effect of band bending at the periphery of the NW. As shown in Figs. 4(g)–4(i), the local spreading resistance mapping of Si-doped GaN NWs exhibits a ring-like maximum intensity in the periphery. This is consistent with the formation of a depleted shell around the conductive core whose effect is to repel the electron free carriers from the edge of the nanowire, which locally increases the resistivity at the periphery. In addition to the formation of this depleted shell, it is also possible that the thin defective shell, which is formed for a Si flux corresponding to a Si concentration above the solubility limit, contributes to decrease the current flow close to the NW sidewalls.[8] Besides, the contrast in SSRM images increased progressively in function of the Si cell temperature. While the spreading resistance at the periphery of NWs is almost constant for the three Si fluxes under consideration [corresponding to pink color in Figs. 4(g)–4(i)], the resistance at the core is decreasing for increasing Si cell temperatures. This indicates that increasing dopant cell temperature enhances Si incorporation in GaN NWs and thereby decreases the resistivity of the core.

By contrast to the previous case of Mg-doped GaN NWs, EDX could not be used for quantitatively determining the Si content in Si-doped NWs due to the use of SiO_2 for the planarization process. Therefore, a SSRM calibration procedure was established for Si-doped GaN NWs. It consists of using a calibration curve, which was constructed by collecting the resistance values of different calibration samples containing known Si dopant concentrations. The GaN calibration samples were grown by metalorganic chemical vapor deposition method on sapphire using a GaN buffer.

Figure 5 provides the schematic presentation and SSRM images of the calibration samples, which were obtained in cross section just after cleaving. Each calibration sample consists of a n-type GaN epi-layer with a known Si dopant concentration and GaN buffer layers. The schematic presentation of calibration samples is displayed in Fig. 5(a). The topography images shown in Figs. 5(b)–5(d) reveal overall flat surfaces. However, some damages can be found at the edge of the samples due to the cleaving. The resistance signals were recorded for n-doped regions of each calibration sample. A clear contrast was observed between the GaN

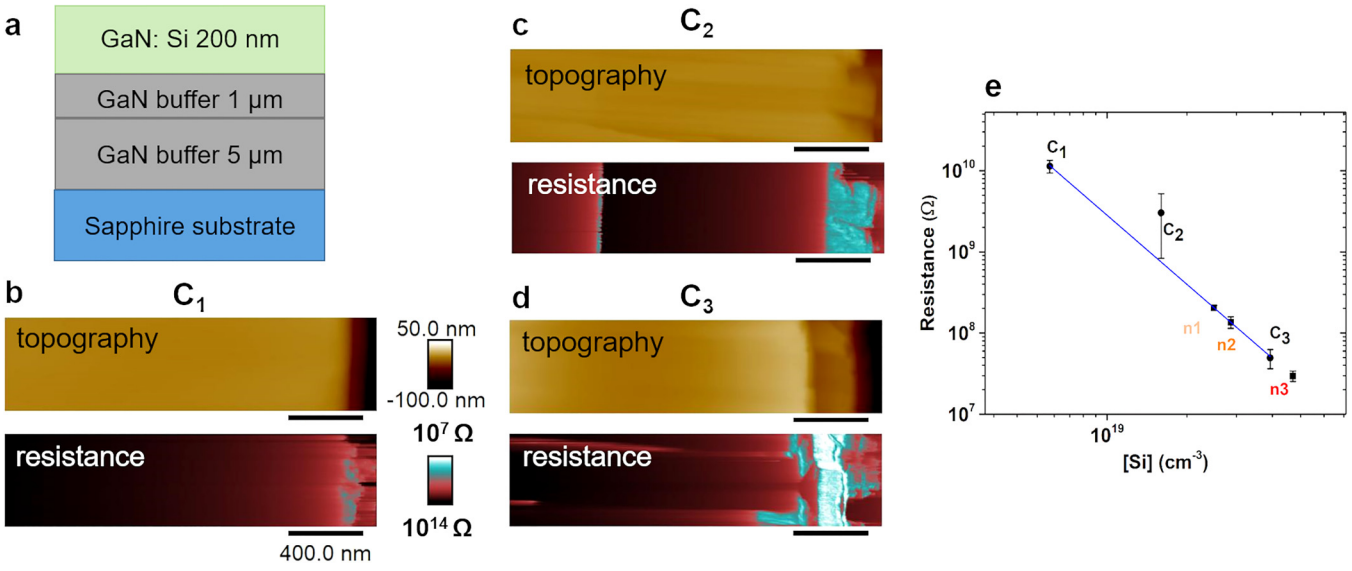

FIG. 5. (a) Schematic cross section and SSRM images of GaN calibration samples. [Si] dopant concentration varied for each sample. (b) C_1, [Si] = 6.5 × 10^{18} cm^{-3}, (c) C_2, [Si] = 1.5 × 10^{19} cm^{-3}, and (d) C_3, [Si] = 3.4 × 10^{19} cm^{-3}. Scale bars = 400 nm. (e) SSRM calibration curve (resistance vs [Si]) extracted from SSRM signal of the calibration samples C_1–C_3 (black dots). Carrier concentration of GaN NWs estimated from linear fit (blue line). GaN NWs with [Si] doping cell temperature of n_1 = 900 °C, n_2 = 920 °C, and n_3 = 938 °C are presented by squares.

TABLE I. Measured SSRM signals of calibration samples and Si dopant concentrations.

Sample	Resistance (Ω)	[Si] (cm^{-3})
C_1	1.1×10^{10}	6.5×10^{18}
C_2	3.0×10^{9}	1.5×10^{19}
C_3	4.9×10^{7}	3.4×10^{19}

buffer layer and the n-doped region. The buffer layers exhibit a high resistance of $\sim 2.5 \times 10^{12}$ Ω in good agreement with its very low residual n-type doping, which is constant and homogeneous for all calibration samples. The SSRM resistances of calibration samples are listed in Table I.

By using these SSRM results, we constructed the calibration curve shown in Fig. 5(e), which is based on a linear correlation between the SSRM resistance signal and the calibrated Si dopant concentration. Once the calibration samples were analyzed, the NWs samples were examined successively using the same AFM probe and in the same experimental conditions. As a matter of fact, variation in the contact force can change the plastic deformation of the sample and so the electrical contact area, which may affect the calibration procedure. Therefore, the imaging parameters were kept constant in order to apply the same force onto the three samples.

We estimated the average carrier concentrations at the core of NWs by measuring the resistance signals at the center of them on SSRM images of each sample. Then, the average carrier concentrations were estimated by linear interpolation on the calibration curve. The results for the three samples are presented in Fig. 5(e) and Table II, assessing the increase in carrier concentration for increasing Si cell temperature.

We further investigated the carrier profile of individual GaN NWs. From these data profiles (resistance vs position along the nanowire diameter), the corresponding carrier concentrations inferred from the resistance values are interpolated using the calibration curve presented in Fig. 5(e) (blue line). The results, shown in Fig. 6, indicate that the carrier concentration at the periphery of nanowires (determined at the profile inflexion points) varies between 1.2 and 1.8×10^{19} cm^{-3}. If now focusing on the NW core, the carrier concentrations are increasing with Si doping and equal to 1.9×10^{19}, $2.8 \times 10^{19-}$, and 4.8×10^{19} cm^{-3} for n_1, n_2, and n_3 samples, respectively. Such a variation is consistent with the increase in Si flux from n_1 to n_3 as we observed previously. Furthermore, the results in Fig. 6(a) show that the difference between shell and conductive core increases for higher Si doping. This core–shell structure can be reasonably assigned to the effect of band bending related to Fermi level pinning on the NW sidewalls. In this case, the size of both the conducting core and the depleted shell are depending on the doping level and on the NW diameter.[27] As the NW diameter does not exhibit large fluctuations for the

TABLE II. Measured SSRM signals of GaN NWs samples and estimated carrier concentrations at the core of nanowire.

Sample	Resistance (Ω)	[Si] (cm^{-3})
n_1	2.0×10^{8}	2.3×10^{19}
n_2	1.4×10^{8}	2.5×10^{19}
n_3	3.0×10^{7}	4.0×10^{19}

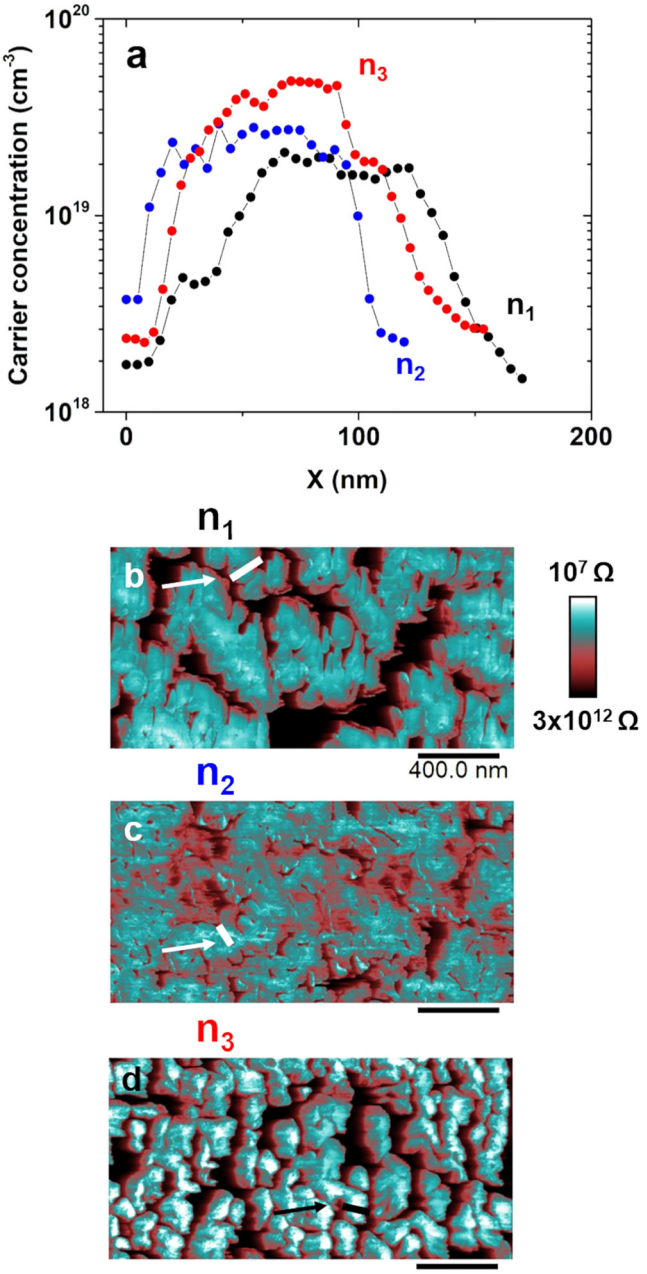

FIG. 6. (a) Calibrated carrier concentration profiles corresponding to the lines indicated in SSRM images. The carrier concentrations were calculated using the calibration curve presented in Fig. 5. SSRM images of GaN NWs samples with Si doping cell temperature of (b) n_1 = 900 °C, (c) n_2 = 920 °C, and (d) n_3 = 938 °C (n_3), respectively. Scale bars = 400 nm.

different samples under scrutiny, the doping level itself is the dominant factor here, which governs the resistivity ratio between core and shell for single NWs.

Besides the formation of a depleted layer due to Fermi level pinning, Fang *et al.* previously observed a higher Si concentration at the periphery (6.5×10^{20} at/m^3) than in the core (2.5×10^{20} at/m^3) of GaN NWs with an overall thickness of the Si-rich shell ranging between 10 and 40 nm.[8] Here, we measured a high resistive shell (low carrier concentration) in the 20–36 nm thickness range. Our findings are consistent with the results of Fang *et al.*, suggesting that for the highest Si flux value the core–shell structure put in evidence by SSRM measurements could be amplified by the accumulation of crystallographic defects in the peripheral zone of the NWs due to the Si doping level above the solubility limit.

III. CONCLUSION

Using SSRM, we have mapped the local resistance of both n-type (Si-doped) and p-type (Mg-doped) GaN NWs at the nanoscale. We have put in evidence the formation of a depleted shell, assigned to Fermi level pinning on the NW sidewalls. In the case of n-type NWs, the formation of a defective shell for Si doping levels beyond the solubility limit may contribute to the formation of the resistive layer. Similarly, in the case of Mg-doped NWs, the formation of a depleted shell is expected. However, in this last case, the inhomogeneous Mg distribution along the NW radius and the peripheral enhancement of the Mg content leads to the formation of a highly conductive shell, which partly counterbalances the effect of the depleted layer associated with Fermi level pinning. Then, it appears that the dopant incorporation regime observed in the case of GaN NWs, namely, a radially inhomogeneous dopant distribution related to the strain relaxation mechanisms specific to NWs, governs to a large extent their electrical transport properties at the nanoscale. Besides considerably affecting the electrical transport properties of GaN NWs, the dopant inhomogeneous distribution should predictably affect the properties of future NW-based opto-electronical devices. Indeed, the NW-specific dopant incorporation regime is a general feature drastically differentiating them from the case of layers.

In this context, the ability of the SSRM technique to provide a quantitative analysis of dopant profiles at the nanoscale underlines the great potential of AFM electrical modes to study and predict the electrical transport properties of NW semiconductors, opening a new way toward their full use for the development of optoelectronic devices.

SUPPLEMENTARY MATERIAL

See the supplementary material for planarization process of nanowire samples, EDX measurements, and AFM/SSRM additional measurements details.

ACKNOWLEDGMENTS

The authors acknowledge the Région Auvergne Rhône Alpes for financial support under the "pack ambition recherche convention n° 170112360161617." This work was also partially supported by Agence Nationale de la Recherche (EMOUVAN Project No. -ANR-15-CE24-0006-04). We thank Dr. A. Dussaigne for providing the n-type GaN layers used for calibration. The authors further acknowledge the Consortium Lyon Saint-Etienne de Microscopie (CLYM, No. FED 4092) for access to the microscopes. We thank Dr. David Albertini (INL) for technical support in CLYM platform. Some of the authors (Georges Brémond, Ece N. Aybeke, and Oleksandr Synhaivskyi from INL) would like to thank Professor Joël Bellessa from the Institut Lumière Matière at the University of Lyon for his practical help in using the dip-coating process facilities.

AUTHOR DECLARATIONS

Conflict of Interest

The authors have no conflicts to disclose.

DATA AVAILABILITY

The data that support the findings of this study are available from the corresponding authors upon reasonable request.

REFERENCES

[1]E. Barrigón, M. Heurlin, Z. Bi, B. Monemar, and L. Samuelson, Chem. Rev. **119**, 9170 (2019).
[2]S. Zhao, J. Lu, X. Hai, and X. Yin, Micromachines **11**, 125 (2020).
[3]F. Glas, Phys. Rev. B **74**, 121302 (2006).
[4]S. Raychaudhuri and E. T. Yu, J. Appl. Phys. **99**, 114308 (2006).
[5]K. Kishino, A. Kikuchi, H. Sekiguchi, and S. Ishizawa, "Gallium nitride materials and devices II," Proc. SPIE **6473**, 64730T (2007).
[6]R. Wang, H. P. T. Nguyen, A. T. Connie, J. Lee, I. Shih, and Z. Mi, Opt. Express **22**, A1768 (2014).
[7]X. Liu, B. H. Le, S. Y. Woo, S. Zhao, A. Pofelski, G. A. Botton, and Z. Mi, Opt. Express **25**, 30494 (2017).
[8]Z. Fang, E. Robin, E. Rozas-Jiménez, A. Cros, F. Donatini, N. Mollard, J. Pernot, and B. Daudin, Nano Lett. **15**, 6794 (2015).
[9]A.-M. Siladie, L. Amichi, N. Mollard, I. Mouton, B. Bonef, C. Bougerol, A. Grenier, E. Robin, P.-H. Jouneau, N. Garro, A. Cros, and B. Daudin, Nanotechnology **29**, 255706 (2018).
[10]A.-M. Siladie, G. Jacopin, A. Cros, N. Garro, E. Robin, D. Caliste, P. Pochet, F. Donatini, J. Pernot, and B. Daudin, Nano Lett. **19**, 8357 (2019).
[11]L. M. Mansfield, K. A. Bertness, P. T. Blanchard, T. E. Harvey, A. W. Sanders, and N. A. Sanford, J. Electron. Mater. **38**, 495 (2009).
[12]P. Parkinson, C. Dodson, H. J. Joyce, K. A. Bertness, N. A. Sanford, L. M. Herz, and M. B. Johnston, Nano Lett. **12**, 4600 (2012).
[13]J. Kamimura, P. Bogdanoff, M. Ramsteiner, P. Corfdir, F. Feix, L. Geelhaar, and H. Riechert, Nano Lett. **17**, 1529 (2017).
[14]W. Vandervorst, and M. Meuris, U. S. patent 5,369,372 (1994).
[15]P. De Wolf, J. Snauwaert, L. Hellemans, T. Clarysse, W. Vandervorst, M. D'Olieslaeger, and D. Quaeyhaegens, J. Vac. Sci. Technol. A **13**, 1699 (1995).
[16]P. De Wolf, T. Clarysse, and W. Vandervorst, J. Vac. Sci. Technol. B **16**, 320 (1998).
[17]D. Álvarez, J. Hartwich, M. Fouchier, P. Eyben, and W. Vandervorst, Appl. Phys. Lett. **82**, 1724 (2003).
[18]C. Celle, C. Mouchet, E. Rouvière, J.-P. Simonato, D. Mariolle, N. Chevalier, and A. Brioude, J. Phys. Chem. C **114**, 760 (2010).
[19]X. Ou, P. D. Kanungo, R. Kögler, P. Werner, U. Gösele, W. Skorupa, and X. Wang, Nano Lett. **10**, 171 (2010).
[20]L. Wang, V. Sallet, C. Sartel, and G. Brémond, Appl. Phys. Lett. **109**, 092101 (2016).

[21]R. Mata, K. Hestroffer, J. Budagosky, A. Cros, C. Bougerol, H. Renevier, and B. Daudin, J. Cryst. Growth **334**, 177 (2011).
[22]F. Furtmayr, M. Vielemeyer, M. Stutzmann, J. Arbiol, S. Estradé, F. Peirò, J. R. Morante, and M. Eickhoff, J. Appl. Phys. **104**, 034309 (2008).
[23]J. E. Northrup, Phys. Rev. B **77**, 045313 (2008).
[24]B. S. Simpkins, M. A. Mastro, C. R. Eddy, and P. E. Pehrsson, J. Appl. Phys. **103**, 104313 (2008).
[25]R. Calarco, M. Marso, T. Richter, A. I. Aykanat, R. Meijers, A. v. d. Hart, T. Stoica, and H. Lüth, Nano Lett. **5**, 981 (2005).
[26]R. Calarco, T. Stoica, O. Brandt, and L. Geelhaar, J. Mater. Res. **26**, 2157 (2011).
[27]Y. Calahorra and D. Ritter, J. Appl. Phys. **114**, 124310 (2013).
[28]L. Wang, J. M. Chauveau, R. Brenier, V. Sallet, F. Jomard, C. Sartel, and G. Brémond, Appl. Phys. Lett. **108**, 132103 (2016).
[29]I. S. Fraser, R. A. Oliver, J. Sumner, C. McAleese, M. J. Kappers, and C. J. Humphreys, Appl. Surf. Sci. **253**, 3937 (2007).
[30]S. Brochen, J. Brault, S. Chenot, A. Dussaigne, M. Leroux, and B. Damilano, Appl. Phys. Lett. **103**, 032102 (2013).